Three-Point Dixon Technique for True Water/Fat Decomposition with B_0 Inhomogeneity Correction

G. H. GLOVER* AND E. SCHNEIDER

GE Medical Systems Group, Applied Science Laboratory, P.O. Box 414, Milwaukee, Wisconsin 53201

An enhancement to Dixon's technique is described which can provide error-free decomposition of water and fat proton images even in the presence of off-resonance conditions which result from susceptibility differences, demagnetization, or shim errors. The method uses three measurements with phase shifts of 0, π, and $-\pi$ between the fat and water resonances. The additional information provided by the third measurement is used to calculate an image of the field inhomogeneity in addition to true water and fat images. The signal-to-noise ratio (SNR) in the decomposed images is equivalent to that of a 2.7 NEX acquisition (instead of 3 NEX), yielding an SNR imaging efficiency of 95%. In addition, the B_0 image which is provided may have diagnostic value in its own right. Examples of head and body scans often portray surprisingly large B_0 shifts near interfaces between air or bone and soft tissue. © 1991 Academic Press, Inc.

I. INTRODUCTION

Dixon introduced a technique for decomposing the fat and water components of the proton signal of a subject into two separate images (*1*). His method utilized two acquisitions wherein the phase shift between water and fat signals was adjusted to be 0 and π radians (in-phase and opposed), respectively. By adding and subtracting the two images obtained from these data, a water and a fat image were obtained. Because of difficulties with magnetic field inhomogeneities, magnitude images were used during the processing. This in turn resulted in loss of signal-to-noise ratio (SNR), as well as ambiguous separation of the two components. The technique was generalized by Sepponen *et al.* for objects having more than two spectral components (*2*). Others have applied selective saturation or selective excitation techniques (*3–9*) to provide water-only or fat-only images.

The Dixon decomposition above is error-free only when chemical shift between the two components is the only source of off-resonance signals (*1*). When field inhomogeneities are present, the accuracy of the decomposition is diminished since the algorithm can not separate phase shifts caused by B_0 errors from those deriving from the fat/water chemical shift. In such cases, the two images are no longer "pure," and suffer bleed-through of the unwanted components in concert with the background field off-resonance.

---

* Present address: Dept. of Diagnostic Radiology, Stanford University School of Medicine, Stanford, CA 94305.

Field inhomogeneities can be generated by gross shim misadjustment, but are more typically caused by morphologically generated demagnetization effects, in which air/tissue or bone/tissue interfaces can cause large local field distortions (10, 11). These local gradients cannot be shimmed out and therefore cause failure of both selective "fat saturation" and Dixon methods in such regions. Figure 1 shows an example of a selective fat saturation experiment in which the suppression is impaired because of local B_0 inhomogeneity. As may be seen, a linear shim applied via an *in vivo* shimming technique (11) does not have sufficient spatial agility to compensate the higher-order B_0 variations over the entire field of view.

In response to the difficulty of removing these local anatomically generated B_0 errors by shimming, previous workers made corrections to the complex data for the field error using second echoes (12), or local phase-unwrap (13) methods. The former method precludes multiple echo imaging, while the latter used phase data from a phantom scan as part of the correction for local inhomogeneities, and is not robust. Recently, a three-point Dixon method was described (14). In this technique, a third measurement with fat/water phase shift of $-\pi$ was added in order to calculate the field error in each pixel and provide an accurate decomposition of the fat and water images. This method provides the background phase reference by assuming a slowly

FIG. 1. (A) "Fat saturation" image, and (B) corresponding B_0 image, with linear *in vivo* shim generated from least-squares fit over full field of view (FOV). Inhomogeneity is too large to suppress fat uniformly (note arctangent wraparounds). (C) Fat saturation image, and (D) corresponding B_0 image, after *in vivo* shim using least-squares fit over a localized FOV near left ear (11). Suppression is improved in target region at expense of other areas.

varying spatial distribution. Under conditions of large resonance offset, however, the approach fails to provide unambiguous decomposition of the two components because of uncertainties with added factors of 2π in the arctangent function.

In the present paper, extensions to the basic algorithm have been applied in order to resolve the phase-unwrap ambiguity. These extensions comprise the addition of a "phase-switch" function and a robust method of phase-unwrapping. The new three-point method has proven useful even when there is substantial susceptibility-generated B_0 inhomogeneity as, for example, near the posterior neck at the cervical spine level.

II. THREE-POINT METHOD

The method relies on acquisition of three separate images under specified conditions of off-resonance phase encoding, and is an extension of the two-point technique (*1*). The encoding of resonance offset information is accomplished in a spin-echo sequence by displacement of the time-reversal (180°) rf pulse from its normal location (centered between the excitation pulse and the echo). Only phase differences between the acquisitions are important; therefore a gradient-recalled sequence can also be employed using differing TEs if the T2 of the tissue being imaged is long compared to the required echo time differences.

A. Technique

With reference to the pulse sequence in Fig. 2, suppose three images (S_0, S_1, S_{-1}) are obtained with the position of the 180° pulse at 0, τ, and $-\tau$, respectively. Furthermore, let the time displacement τ be adjusted such that

$$\omega_{cs}\tau = \pi/2,\qquad\qquad [1]$$

where ω_{cs} is the chemical shift of fat with respect to water. In this case, acquisitions of signals that are off-resonance by an amount ω contain a phase shift $\phi = 2\omega\tau = (\omega/\omega_{cs})\pi$. If the spectrometer is adjusted so that the water signal is on-resonance, then S_1 and S_{-1} are redundant since each gives equivalent fat-opposed images. However, if there is a field offset present, these two measurements are not redundant and provide information which may be used to calculate the resonance offset error and correct the decomposition. We have for each pixel in the three images (*15*)
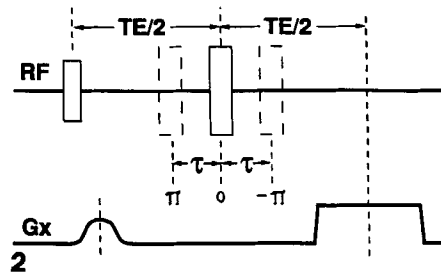

FIG. 2. Spin-echo pulse sequence for three-point method. Resonance offset is encoded by changing the position of the 180° rf pulse for the three acquisitions. Pulses are shown schematically for clarity; sinc waveforms are actually used.

$$S_0 = (\rho_1 + \rho_2)e^{i\phi_0}, \tag{2}$$

$$S_1 = (\rho_1 - \rho_2)e^{i(\phi+\phi_0)}, \tag{3}$$

$$S_{-1} = (\rho_1 - \rho_2)e^{-i(\phi-\phi_0)}, \tag{4}$$

where ρ_i are the (real) amplitudes of the water and fat components which we would like to determine, and

$$\phi = \omega_0\tau = \pi\omega_0/\omega_{cs}, \tag{5}$$

where ω_0 is an unknown off-resonance frequency resulting from field error, and ϕ_0 is a phase offset resulting from rf penetration effects and other systematic phase shifts. ϕ_0 depends on location, but is independent of chemical shift. It is convenient to remove ϕ_0 by determining it from [2] as the argument of S_0. Then

$$S_0' \equiv S_0 e^{-i\phi_0} = \rho_1 + \rho_2, \tag{6}$$

$$S_1' \equiv S_1 e^{-i\phi_0} = (\rho_1 - \rho_2)e^{i\phi}, \tag{7}$$

$$S_{-1}' \equiv S_{-1} e^{-i\phi_0} = (\rho_1 - \rho_2)e^{-i\phi}. \tag{8}$$

We note that [7] and [8] are redundant only when $\phi = 0$. A solution to [6]–[8] is formally obtained as

$$\rho_1 = (S_0' + p\sqrt{S_1' S_{-1}'})/2,$$
$$\rho_2 = (S_0' - p\sqrt{S_1' S_{-1}'})/2, \tag{9}$$

where $p = \pm 1$ is a switch function which contains the sign of the complex square root. Thus if the correct sign can be chosen, ρ_1 and ρ_2 can be found despite the presence of B_0 errors.

The choice of sign (p) in [9] was found to be troublesome in previous work (15). Consider the case when a pixel contains just water ($\rho_2 = 0$). Then we must choose $p = +1$ so that

$$\rho_1 = (S_0' + \sqrt{S_1' S_{-1}'})/2,$$
$$\rho_2 = (S_0' - \sqrt{S_1' S_{-1}'})/2, \tag{10}$$

as may be seen from [6]–[8]. On the other hand, if a pixel contains only fat, the opposite sign must be used. Thus some additional constraint must be used to determine p.

We now present a means of determining the sign. From [8], if ϕ were known the sign of $\rho_1 - \rho_2$, and thus p, could be determined from $\arg(S_{-1}' e^{i\phi})$. Consider

$$g \equiv S_1 S_{-1}^* = |\rho_1 - \rho_2|^2 e^{i2\phi}. \tag{11}$$

Note that ϕ may be uniquely determined from $\phi_m = \arg(g)$ only if $|\phi| \le \pi/2$, since ϕ_m is unambiguous only between $-\pi$ and π, as shown in Fig. 3a. Unfortunately this condition is too restrictive since it would limit the useful offset frequency range to $\pm\omega_{cs}/2$. A method has been developed to extend the range of ϕ beyond $\pi/2$. This algorithm contains two steps.
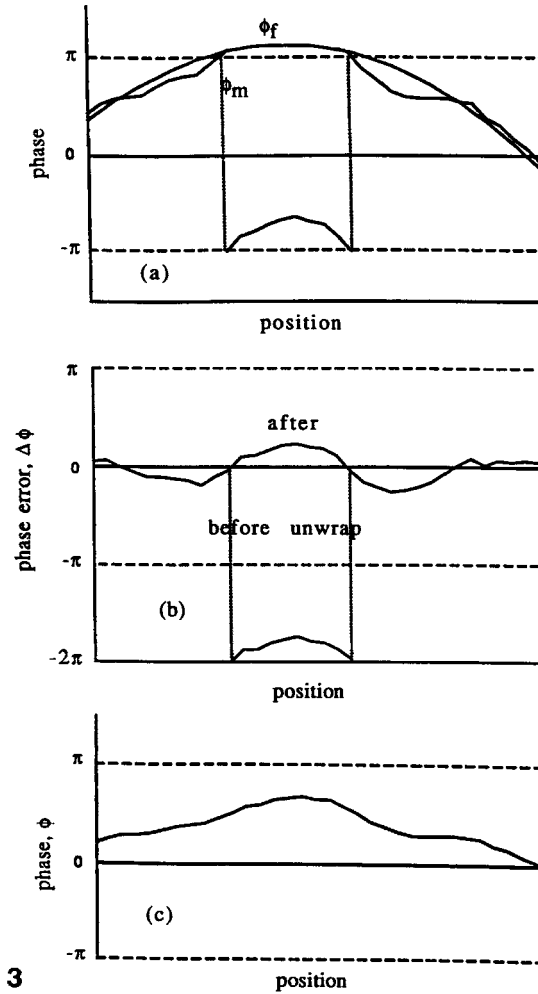
FIG. 3. Steps in determination of ϕ. See Appendix 1. (a) Measured (ϕ_m) and fit (ϕ_f) phase, showing 2π wraparound in ϕ_m. (b) 2π discontinuities in fit error, $\Delta\phi$, may be easily removed. $|\Delta\phi|$ is then $<\pi$, and the square root is unambiguous. (c) $\phi = \phi_f/2 + \Delta\phi/2$. Compare with $\phi_m/2$.

The details of the first portion of the technique are presented in Appendix 1; a summary is given here. A bicubic polynomial $\phi_f(x, y)$ is first fit to $\phi_m = \arg(g)$. This is accomplished by fitting to spatial derivatives of ϕ_m, for which it is easy to recognize and discard the 2π discontinuities. Then ϕ_f is subtracted from ϕ_m while multiples of 2π are unambiguously removed; the resulting difference phase is halved (equivalent to taking the complex square root), and $\phi_f/2$ is added on again afterward. In this way the square root required in [11] to extract ϕ is uniquely determined for a range of offsets between $\pm\omega_{cs}$. This algorithm works fairly well on its own, but it fails in regions of localized high inhomogeneity, where the cubic function is not able to follow the spatially rapid perturbation, or where wraparounds beyond 2π are encountered.

A second step which uses trend analysis is therefore applied to follow the remaining wraparound points.

The trend analysis algorithm uses a modified exponentially smoothing estimate of the next point in a line of pixels from some fraction of the past points. The modification is that the update to the estimate only uses phase information for pixels where the complex magnitude is significant. In this way the trend continues across "holes" in the object so that phase continuity is preserved even in these difficult cases. A detailed description is presented in Appendix 2.

This combined method of subtracting the low-order function and then correcting by trend analysis has been found to be robust.

With ϕ known, a switch angle θ can be found from [8]:

$$\theta = \arg(S'_{-1}e^{i\phi}).$$ [12]

Note that θ will be approximately 0 or π, depending upon the predominance of ρ_1 over ρ_2. A continuous "switch function" p may now be chosen as

$$p = \cos\theta,$$ [13]

since $\cos\theta \approx 1$ if $\rho_1 > \rho_2$ and -1 if $\rho_1 < \rho_2$. The continuity of p is important in avoiding artificial contouring at fat/water borders. Hence we may take the final solution as

$$\rho_1 = (S'_0 + \cos\theta\sqrt{S'_1S'_{-1}})/2$$

$$\rho_2 = (S'_0 - \cos\theta\sqrt{S'_1S'_{-1}})/2.$$ [14]

B. Noise Performance

We calculate the signal-to-noise ratio of this technique relative to that for a single acquisition (1 NEX) scan. For the water image (dropping the primes for convenience),

$$\rho_1 = \rho_1(S_0, S_1, S_{-1}).$$ [15]

The noise variance in ρ_1 may be calculated with the assumption that the three measurements are uncorrelated. Then

$$\sigma_{\rho_1}^2 = \left|\frac{\partial\rho_1}{\partial S_0}\right|^2 \sigma_{S_0}^2 + \left|\frac{\partial\rho_1}{\partial S_1}\right|^2 \sigma_{S_1}^2 + \left|\frac{\partial\rho_1}{\partial S_{-1}}\right|^2 \sigma_{S_{-1}}^2.$$ [16]

From [14],

$$\left|\frac{\partial\rho_1}{\partial S_0}\right|^2 = 1/4.$$ [17]

The second term in [16] is

$$\frac{\partial\rho_1}{\partial S_1} = 1/4 \cos\theta(S_{-1}/S_1)^{1/2} - 1/2(S_1S_{-1})^{1/2}\sin\theta \frac{\partial\theta}{\partial S_1}.$$ [18]

Since $\theta \approx 0$ or π, the second term in [18] is nearly 0. This means that the $\cos\theta$ switch function is essentially noiseless. This was verified experimentally by reconstructing an image of $\cos\theta$. Then, since $|S_{-1}| = |S_1|$,

$$\left|\frac{\partial \rho_1}{\partial S_1}\right|^2 = 1/16, \tag{19}$$

with an identical value for $|\partial \rho_1 / \partial S_{-1}|^2$.

Now we assume that all measurements have the same variance ($\sigma_S \equiv \sigma_{S_0} = \sigma_{S_1} = \sigma_{S_{-1}}$). Then, [16], [17], and [19] yield

$$\sigma_{\rho_1}^2 = \frac{1}{4} \sigma_S^2 + \frac{1}{16} \sigma_S^2 + \frac{1}{16} \sigma_S^2$$

$$= \frac{3}{8} \sigma_S^2, \tag{20}$$

or

$$\sigma_{\rho_1} = 0.61 \sigma_s. \tag{21}$$

The noise of the three-point method is equivalent to that of an $\frac{8}{3} = 2.67$ NEX acquisition. The added measurements produce nearly the full additional SNR in the water or fat image that is expected from a conventional 3 NEX scan. Some loss is expected because the added resolution in the chemical shift direction must increase the variance in the amplitude estimates. An imaging efficiency may be calculated based on the SNR relative to that for a conventional 3 NEX scan:

$$\zeta = \sqrt{8/3}/\sqrt{3} = 0.95. \tag{22}$$

Thus the penalty paid for recovering the unknown susceptibility/shim error information is rather slight.

It is instructive to examine the use of the three-point technique as a means of removing chemical shift artifact. In such a proposed technique, the three-point decomposition is performed, the fat image is shifted in the frequency direction by the correct number of pixels to register it with the water image, and the two images are then added. The result is a standard (in-phase) image of both components with the pixel offset removed. Let us calculate the SNR of the recombined water/fat image to examine the viability of this approach. Rather poor performance might be predicted, since combination of ρ_1 and ρ_2 with no pixel shift gives (from Eq. [14] $\rho_1 + \rho_2 = S_0'$, which is just the original 1 NEX, in-phase image.

With pixel shift of the second image (denoted with a prime), the signal is $\rho_1 + \rho_2'$. The variance is $\sigma_{\rho 1}^2 + \sigma_{\rho 2}^2 + 2\langle(\rho_1 - \overline{\rho_1})(\rho_2' - \overline{\rho_2'})\rangle$, where the brackets denote expectation, and the bars denote average. The last term can be shown to be small if the chemical shift, in pixels, is small. Then $\sigma_{\rho_c}^2 \approx \sigma_{\rho_1}^2 + \sigma_{\rho_2}^2$, so that $\sigma_{\rho_c} = 0.87\sigma_s$, for an efficiency of 67%; this corresponds to an averaging equivalence of 1.33 NEX.

III. EXPERIMENTAL RESULTS

A multiplanar, spin-echo pulse sequence was written to obtain the three acquisitions in one scan. The sequence uses slice plane as the inner loop, then resonance offset encode (position of the 180° rf pulse) as the next loop, and finally phase encode as the outer loop. The resulting three echo data were reconstructed by an on-line program to obtain the water, fat, and B_0 images. The scans were performed with a 1.5-T magnet

(GE SIGNA). The shim measured with water phantoms showed homogeneity better than 0.5 ppm for both head and body fields of view.

Figures 4–6 show results using the new algorithm. In each case a 1 NEX standard image (the in-phase acquisition), a water image, fat image, and B_0 image are shown. As may be seen, complete suppression of the unwanted signal is achieved in the fat and water images despite significant anatomy-generated B_0 inhomogeneity. This holds even in the sagittal image (Fig. 5), where there is nearly complete loss of signal near the nasal cavity. Note that the motion artifacts are reduced in the body scan as expected by the averaging. Because of arbitrary phasing of the breathing motion relative to the pulse sequence triggering, however, the fat ghosts may appear in either the fat or water image.

The ratio of noise in the three-point method vs a 1 NEX image was measured for gray matter in the head (Fig. 4), giving $\sigma_3/\sigma_1 = 0.74$, while in the air outside the head $\sigma_3/\sigma_1 = 0.58$. The discrepancy with the expected ratio of 0.61 in the brain is not fully understood. However, the noise measurements were difficult to make because the image intensities were not flat.

The water and fat images in Fig. 5 were combined with a shift of two pixels in the readout direction of the fat image (1.67 pixels was the exact chemical shift value). The resulting image had $\sigma_c/\sigma_1 = 0.92$ in the ventricle, and $\sigma_c/\sigma_1 = 0.78$ in the air outside the head. These values are to be compared with the expected ratio of 0.87.
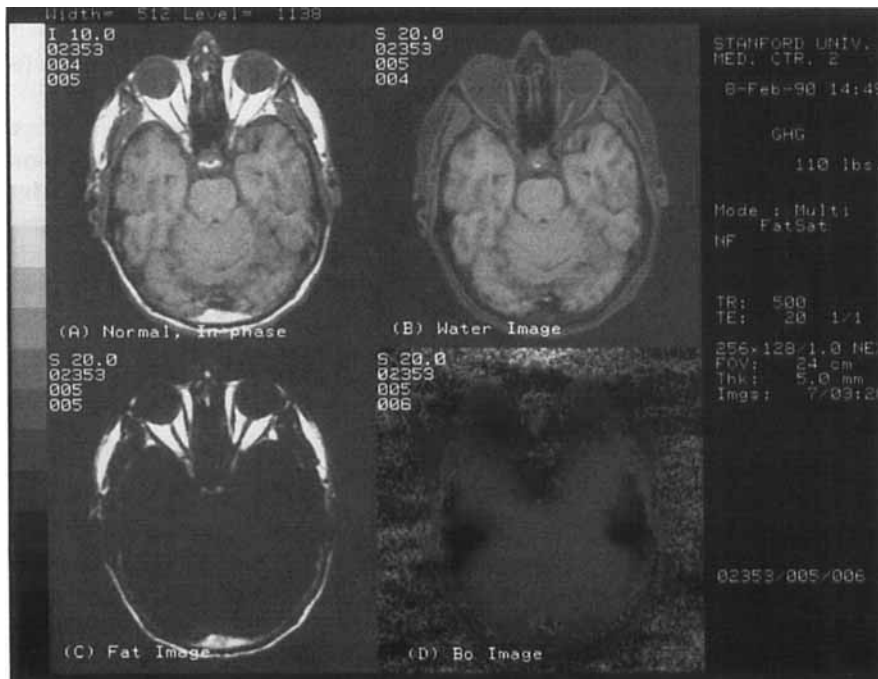

FIG. 4. Axial image of normal volunteer. (A) Conventional in-phase image, (B) water image, (C) fat image, (D) B_0 image. Note large (3 ppm) decrease in B_0 near auditory canals from susceptibility differences, and improved visualization of optic nerves in water image.
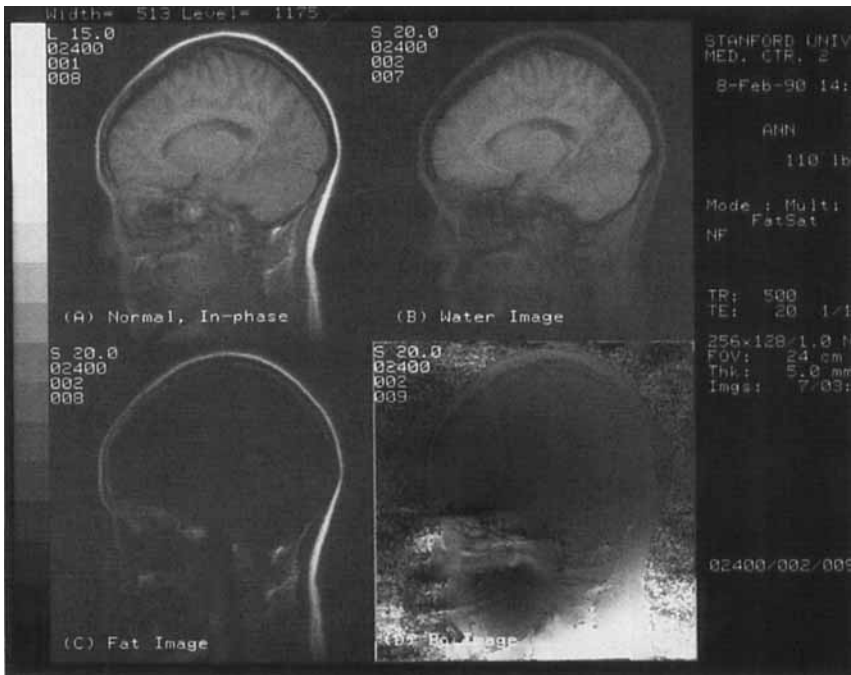
FIG. 5. Sagittal image of normal volunteer as in Fig. 4 showing lipid content near orbit. B_0 variation from brain to posterior neck is >6 ppm. Note that phase continuity is maintained across low signal regions near nasal cavity.

IV. DISCUSSION

The three-point technique has been shown to yield unambiguous separation of the fat and water components even in cases where the B_0 offset is greater than the chemical shift. As can be seen in the sagittal head images, there may be a few instances where air–tissue susceptibility differences generate local field gradients so large that the phase unwrap algorithm fails, however. In these instances the fat and water components are interchanged. Our experience has been that these errors are not significant, especially as the susceptibility image is provided and may be used to verify the decomposition.

The alignment of the two-component spectrum relative to the spectrometer center frequency determines which of the images (ρ_1, ρ_2) portrays the water component and which is the fat image. If the water component is placed on-resonance, then ρ_1 is the water image, and vice versa. However, the algorithm will remove resonance offsets by incorporating them in the B_0 image. If the offset is less than half the chemical shift, the water and fat images remain in the correct order; i.e., ρ_1 is the water image and ρ_2 is the fat image. For offsets greater than this amount the image assignment is reversed. In any case, the decomposition is still complete (no intermixing of components within an image).

We have found instances in multislice scanning where the B_0 offset varies sufficiently along the slice location direction that the image order switches from one slice to the
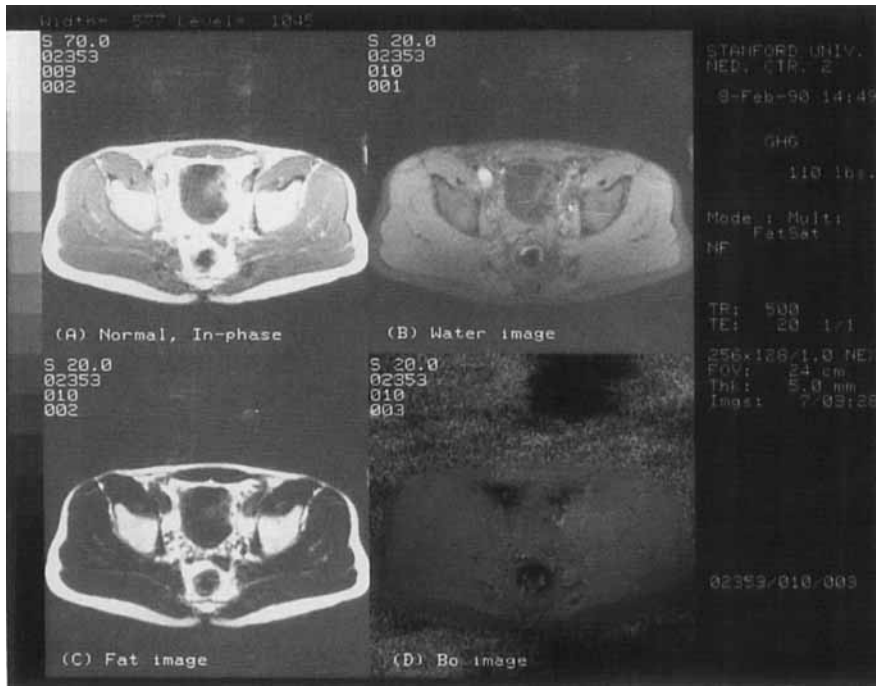
FIG. 6. Pelvic scan as in Fig. 4, showing structure in bone marrow not easily appreciated in conventional image.

next. This could be mitigated by using the *in vivo* shim technique (*11*) first to remove these low-order, subject-dependent field offsets.

The SNR of this decomposition is essentially that of a 2.7 NEX acquisition although the scan time corresponds to 3 NEX. This leads to a rather remarkable SNR efficiency of 95%. This small penalty is worth accepting because an unambiguous fat/water resolution is obtained, and because a susceptibility image is also provided. The latter image may have diagnostic information as well, as, for example, in cases of hematomas where the iron can produce substantial local field abberations.

It was shown that recombining the decomposed images to produce a chemical shift-free image is not very efficient from an SNR point of view. In fact the resulting image has SNR equivalent to only a $\frac{4}{3}$ NEX image.

The pulse sequence shown in Fig. 2 and used in this work is a multiplanar spin-echo version. A GRASS-type sequence could be used by gathering the three acquisitions with differing TEs ($\Delta TE = 2\tau \approx 2.4$ ms). Since the echo time differences are small, little effect from T2 decay is expected.

APPENDIX 1: PHASE CORRECTION BY POLYNOMIAL SUBTRACTION

In this technique, a low-order polynomial is fit to ϕ, and the resulting function is subtracted from ϕ before the square root. If the fit is reasonably good, the argument

of the square root $<\pi/2$ so that the branch point is well determined. Following the square root, the polynomial function is added back to yield an unambiguous map of ϕ.

Let

$$
\begin{aligned}
g(x, y) &= f(x, y)e^{i\phi_m(x,y)} \\
&= f(x, y)e^{i2\phi(x,y)} \\
&= f(x, y)e^{i[\phi_f(x,y)+\Delta\phi]},
\end{aligned}
\qquad [A1.1]
$$

where

$$
\phi_f(x, y) = \sum_{n=1}^{3} [a_n(x - x_0)^n + b_n(y - y_0)^n] + c_0
\qquad [A1.2]
$$

is a polynomial to be fit to the phase of $g(x, y)$, (x_0, y_0) is the center of gravity of the magnitude image for the in-phase acquisition, and $\Delta\phi$ is the error resulting from the fit. A convenient method of performing this fit is that employed previously (11), where weighted least-squares fits are performed on the derivative of $\arg(g(x, y))$ sequentially in the x and y directions to obtain the a's and b's. In this method, $p_3(x - x_0)^2 + p_2(x - x_0) + p_1$ is fit to $d\phi_m/dx$. This fit is obtained by standard weighted least-squares techniques, where the weight is chosen to be $|g(x, y)|$. The derivative is taken because the discontinuities in arc-tangent wraparound points can easily be recognized and removed from the least-squares procedure. With the p's determined, the coefficients (a, b) are found by explicit integration as

$$
p_1 = a_1 - 2a_2x_0 + 3a_3x_0^2
\qquad [A1.3]
$$

$$
p_2 = 2a_2 - 6a_3x_0
\qquad [A1.4]
$$

$$
p_3 = 3a_3.
\qquad [A1.5]
$$

A similar procedure is applied to obtain the b coefficients from $d\phi'/dy$.

Once the (a, b) coefficients, and therefore ϕ_f, is known, we have

$$
2\phi = \phi_f + \Delta\phi,
\qquad [A1.6]
$$

and thus the function

$$
h = ge^{-i\phi_f} = |\rho_1 - \rho_2|^2 e^{-i\Delta\phi}.
\qquad [A1.7]
$$

Now we may assume that any values of $|\Delta\phi| > 2\pi$ result from wraparounds which can be unambiguously removed. Thus if $|\Delta\phi| > 2\pi$ we set $\Delta\phi = \Delta\phi - \text{sgn}(\Delta\phi)*2\pi$. Then, $h^{1/2}$ is uniquely determined, so that

$$
\begin{aligned}
e^{i\phi} &= e^{i\phi_f/2}e^{i\Delta\phi/2} \\
&= (S_1 S_{-1}^* e^{-i\phi_f})^{1/2} e^{i\phi_f/2}/|\rho_1 - \rho_2|.
\end{aligned}
\qquad [A1.8]
$$

Thus the field inhomogeneity ϕ can be obtained from [A1.8]. These steps are illustrated in Fig. 3.

GLOVER AND SCHNEIDER

APPENDIX 2: PHASE UNWRAPPING ALGORITHM USING TREND ANALYSIS

The phase unwrapping algorithm is shown in Fig. A2.1. The algorithm begins by finding the center of gravity (C of G) of the amplitude image from the in-phase image, $A(x, y)$. At this y value, the maximum amplitude is found for the line. A starting phase value is found at this point using a weighted average. During the averaging, care must be taken that wraparounds do not occur. This is assured by averaging in a small box using two values of phase offset $(0, \pi)$ to move the wraparound point, and comparing the resulting standard deviation of the two averages. The result with the lowest deviation, after correction for the offset, is chosen.
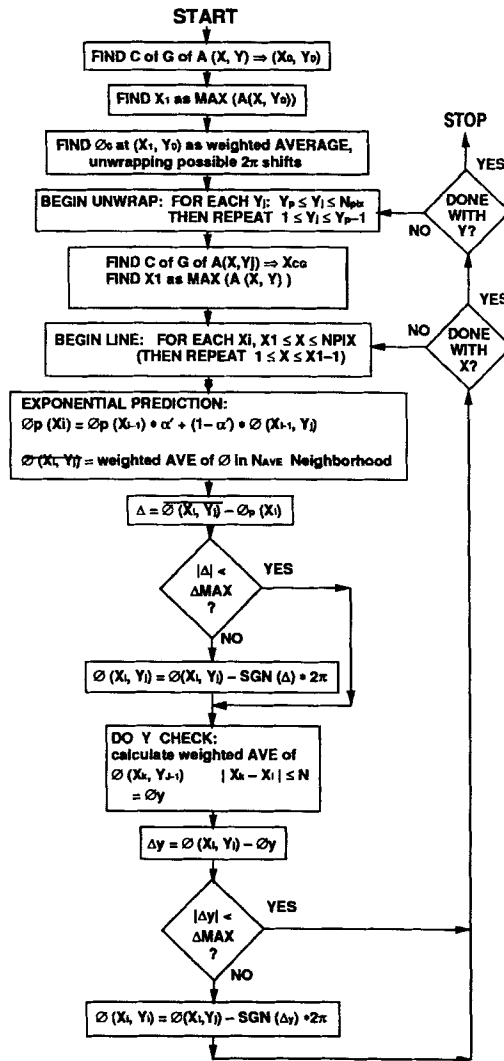

FIG. A2.1. Phase unwrap algorithm using trend analysis.

The unwrapping then begins at the C of G y line and works down to the bottom of the image; when finished the top of the image is unwrapped starting one line above the C of G y line. For each such y line, an $x1$ is chosen as the maximum of $A(x, y)$ in the interval between the center of gravity for that y line and the image boundary. The line is then unwrapped from $x1$ to the boundary, NPIX. After unwrapping this half of the line, the other half is similarly unwrapped.

The line unwrapping uses exponential prediction (trend analysis) to estimate the phase value to be expected at a given x. The algorithm for the trend analysis is described as follows. Let $\phi(i)$ be the phase of the ith pixel in a line, $A(i)$ the complex magnitude, α a fixed parameter (currently 0.6), and A_{max} the maximum of $A(i)$ for the line. Then we may predict the expected phase $\phi_p(i)$ for the ith pixel from previous estimates $\phi_p(i-1)$ and the phase at that pixel $\phi(i)$ from

$$\phi_p(i) = (1 - \alpha')\phi(i) + \alpha'\phi_p(i-1), \qquad [A2.1]$$

where

$$1 - \alpha' = (1 - \alpha)A(i)/A_{max}. \qquad [A2.2]$$

As may be seen from [A2.2], if $A(i)$ is very small, then $1 - \alpha'$ is small, and the prediction $\phi_p(i)$ uses very little of the local phase information but instead continues the previous prediction $\phi_p(i) = \phi_p(i-1)$. This assures that the same trend is continued across amplitude "holes" in the object.

This prediction is compared to a weighted average of the input phase. If the difference $|\phi_p(i) - \phi(i)|$ is too large, it is assumed a 2π phase wrap has occurred, and a corresponding factor of 2π is added. Next a check is made that the corrected value is consistent with a weighted average of the phase in the preceding line; if the difference is too large, a factor of 2π is added.

ACKNOWLEDGMENTS

REFERENCES

1. W. T. DIXON, Radiology 153, 153 (1984).
2. R. E. SEPPONEN, J. T. SIPPONEN, AND J. I. TANTTU, J. Comput. Assist. Tomogr. 8, 585 (1984).
3. B. R. ROSEN, V. J. WEDEEN, AND T. J. BRADY, J. Comput. Assist. Tomogr. 8, 813 (1984).
4. D. N. GUILFOYLE AND P. MANSFIELD, Magn. Reson. Med. 2, 479 (1985).
5. A. HAASE AND J. FRAHM, J. Magn. Reson. 64, 94 (1985).
6. A. HAASE, J. FRAHM, W. HANICKE, AND D. MATTHAEI, Phys. Med. Biol. 30, 341 (1985).
7. P. M. JOSEPH, J. Comput. Assist. Tomogr. 9, 651 (1985).
8. E. YAMAMOTO AND H. KOHNO, IEEE Trans. Med. Imaging 3, 713 (1986).
9. P. J. KELLER, W. W. HUNTER, AND P. SCHMALBROCK, Radiology 164, 539 (1987).
10. K. M. LUDEKE, P. ROSCHMANN, AND R. TISCHLER, Magn. Reson. Imaging 3, 329 (1985).
11. G. H. GLOVER AND E. SCHNEIDER, Magn. Reson. Med., in press.
12. H. N. YEUNG AND D. W. KOROMOS, Radiology 159, 783 (1987).
13. J. A. BORRELLO, T. L. CHENEVERT, C. R. MEYER, A. M. AISEN, AND G. M. GLAZER, Radiology 164, 531 (1987).
14. C. C. LODES, J. P. FELMLEE, R. L. EHMAN, C. M. SEGHAL, J. F. GREENLEAF, G. H. GLOVER, AND J. E. GRAY, J. Comput. Assist. Tomogr. 13, 855 (1989).